Research Square

Preprints are preliminary reports that have not undergone peer review.
They should not be considered conclusive, used to inform clinical practice,
or referenced by the media as validated information.

Comparative proteomics reveals distinct architecture-associated states in spheroid and bioprinted cervical cancer models

Pablo Saldivia
University of Concepción
Carla Villavicencio
University of Concepción
María J. Leiva-Carrasco
University of Concepción
Francisco Verdugo-Avello
San Sebastián University
Sergio Hernández
MELISA Institute
Rodrigo Luengo
University of Concepción
Esteban Gutiérrez
Hospital Regional de Concepción
Rodrigo San Martín
Hospital Regional de Concepción
Mauricio Hernández
MELISA Institute
Jorge R. Toledo
jotoledo@udec.cl

University of Concepción

Article

Keywords: Cervical cancer, spheroids, 3D bioprinting, DIA-PASEF proteomics, cell-matrix interaction, metabolic remodeling

Posted Date: November 12th, 2026

DOI: https://doi.org/10.21203/rs.3.rs-11446584/v1

License: This work is licensed under a Creative Commons Attribution 4.0 International License.
Read Full License

Additional Declarations: No competing interests reported.

Comparative proteomics reveals distinct architecture-associated states in spheroid and bioprinted cervical cancer models

Pablo Saldivia[1,2], Carla Villavicencio[1], María J. Leiva-Carrasco[1], Francisco Verdugo-Avello[6,1], Sergio Hernández[3], Rodrigo Luengo[4], Esteban Gutiérrez[5], Rodrigo San Martín[5], Mauricio Hernández[3]*, Jorge R. Toledo[1]*

[1]Laboratorio de Biotecnología y Biofármacos, Departamento de Fisiopatología, Facultad de Ciencias Biológicas, Universidad de Concepción, Concepción, Chile.

[2]Fundación de Investigación San Ramón (FISAR), San Pedro de la Paz, Chile.

[3]Division of Biotechnology, MELISA Institute, Concepción, Chile.

[4]Departamento de Ingeniería Mecánica, Facultad de Ingeniería, Universidad de Concepción, Concepción, Chile.

[5] Hospital Clínico Regional de Concepción Dr. Guillermo Grant Benavente, Concepción, Chile.

[6] Facultad de Odontología, Universidad San Sebastián, Sede Concepción, Concepción, Chile.

* Correspondence: jotoledo@udec.cl, mhernandez@melisainstitute.org

Tel.: +56 41 266 1037.

Abstract

Three-dimensional cancer models are widely used to improve the biological relevance of *in vitro* studies, yet scaffold-free spheroids and hydrogel-supported bioprinted constructs are often grouped under the same "3D" category. Here, we compared HeLa and SiHa cervical cancer cells cultured as adherent monolayers, scaffold-free spheroids, and 3D bioprinted alginate/gelatin constructs. Morphology, resazurin-based relative metabolic activity, and DIA-PASEF label-free quantitative proteomics were integrated with differential protein abundance analysis, pathway enrichment, direct 3D-to-3D comparison, and selected protein-level assessment. The global proteomic dataset comprised 8,837 protein groups and showed architecture-dependent organization in both cell lines. Spheroid and bioprinted models differed morphologically and metabolically and diverged markedly from adherent cultures at the proteome level. Spheroids were preferentially associated with glycolytic remodeling, metabolic adaptation, and hypoxia-associated signatures, compatible with compact multicellular organization and diffusion-limited architecture. In contrast, bioprinted

models showed greater representation of ECM/cell-matrix-associated proteins and selected extracellular-remodeling proteins. Direct 3D-to-3D comparison confirmed that spheroid and bioprinted architectures generated distinct proteomic states. These findings support proteome-informed selection of 3D models according to the biological question under investigation.

Keywords: Cervical cancer; spheroids; 3D bioprinting; DIA-PASEF proteomics; cell-matrix interaction; metabolic remodeling

1. Introduction

Cervical cancer remains one of the most important malignancies affecting women worldwide, despite being largely preventable through vaccination, screening, and early treatment of precursor lesions. Recent global estimates indicate that cervical cancer accounts for more than 660,000 new cases and approximately 350,000 deaths annually, ranking among the leading causes of cancer-related morbidity and mortality in women. This burden is unequally distributed, with the highest incidence and mortality rates occurring in regions with limited access to organized screening programs, human papillomavirus (HPV) vaccination, and timely oncological care [1,2]. Persistent infection with high-risk HPV genotypes, particularly HPV16 and HPV18, is the main etiological driver of cervical carcinogenesis [3]. However, malignant progression also depends on additional molecular events involving epithelial transformation, immune evasion, extracellular matrix remodeling, metabolic adaptation, and interactions with the local microenvironment.

Experimental models have been essential for understanding cervical cancer biology and evaluating therapeutic vulnerabilities. Among them, HeLa and SiHa cells remain two of the most widely used human cervical cancer cell lines. HeLa cells, derived from cervical adenocarcinoma and associated with HPV18, and SiHa cells, derived from squamous cell carcinoma and associated with HPV16, provide complementary biological contexts for studying HPV-associated cervical cancer phenotypes [4–6]. Nevertheless, most mechanistic and drug-response studies using these models have historically relied on conventional two-dimensional adherent cultures. Although 2D systems are technically simple, reproducible, and compatible with high-throughput assays, they fail to reproduce key features of solid tumors, including three-dimensional architecture, spatial gradients, cell–cell interactions, extracellular matrix engagement, mechanical constraints, nutrient and oxygen diffusion barriers, and microenvironment-associated signaling [7–9].

Three-dimensional culture systems have emerged as more physiologically relevant alternatives to conventional monolayers [9–11]. Spheroids are among the most established 3D models and recapitulate several features of avascular tumor regions, including compact cell aggregation, diffusion-limited gradients, metabolic stress, and hypoxia-associated adaptation [12–15]. In HeLa spheroid and microspheroid models, 3D organization has been associated with constraints on glucose diffusion, glycolytic oscillations, altered energy metabolism, and hypoxia- and hypoglycemia-associated stress responses [16,17]. These features make spheroids particularly useful for studying tumor growth, therapy resistance, and cell survival under constrained microenvironmental conditions. However, spheroids are primarily self-assembled cellular aggregates and do not fully capture the contribution of an externally defined matrix environment.

In contrast, 3D bioprinting enables the controlled spatial deposition of tumor cells within biomaterial scaffolds, thereby generating matrix-embedded tumor models with defined geometry, architecture, and bioink composition. By incorporating hydrogel matrices such as alginate/gelatin, bioprinting provides a strategy to model scaffold-associated cell organization and cell-matrix interaction features that are not fully represented in spheroid cultures [18–20]. In cervical cancer, previous studies largely based on HeLa spheroids or HeLa 3D-printed models have explored 3D culture platforms for tumor modeling, drug testing, and microenvironmental simulation. These studies support the relevance of three-dimensional architecture for modulating cell morphology, relative metabolic activity, proliferation, extracellular remodeling, EMT-associated marker expression, and therapeutic response [21–24]. Nevertheless, most available comparisons have focused on morphology, viability-related readouts, selected molecular markers, transcriptomic signatures, or drug-response assays. The extent to which distinct 3D architectures reshape the global proteomic landscape of cervical cancer cells remains insufficiently characterized.

Mass spectrometry-based proteomics provides a powerful strategy for systematically evaluating cellular states across experimental models [25]. Proteomic profiling has been used to characterize patient-derived tumor organoids and distinguish tumor-associated molecular phenotypes, supporting its value as a benchmarking approach for *in vitro* cancer models [26]. Recent advances in data-independent acquisition, trapped ion mobility spectrometry, and streamlined sample preparation have improved proteomic coverage, quantitative reproducibility, and throughput [27–29]. In this context, label-free DIA-PASEF proteomics offers an opportunity to compare how cervical cancer cells reorganize their proteome in response to different culture architectures. Such

comparisons are important not only for understanding model-specific biology but also for guiding the rational selection of *in vitro* systems in preclinical research. Here, we systematically compared HeLa and SiHa cervical cancer cells cultured as conventional 2D adherent monolayers, 3D spheroids, and 3D bioprinted alginate/gelatin models. We integrated morphological assessment, resazurin-based relative metabolic activity measurements, and DIA-PASEF label-free quantitative proteomics to evaluate architecture-dependent phenotypes. Our analysis shows that 3D architecture strongly reshapes the cervical cancer proteome, with spheroids preferentially associated with metabolic adaptation and hypoxia-associated signatures, whereas bioprinted models show stronger ECM/cell-matrix and selected extracellular-remodeling protein signatures. These findings indicate that spheroid and bioprinted systems are not interchangeable 3D models; rather, they induce distinct proteomic states in cervical cancer cells.

2 Results

2.1 Spheroid and bioprinted architectures differentially shape cervical cancer cell morphology and metabolic activity.

HeLa and SiHa cells were cultured as adherent monolayers (Ad), scaffold-free spheroids (Sp), and 3D-bioprinted constructs (Bp) (Fig. 1A). The workflow integrated model generation, bright-field morphological assessment, resazurin-based relative metabolic activity measurements, and DIA-PASEF proteomics. At 168 h, microscopy revealed marked architecture-dependent differences in cellular organization (Fig. 1B).

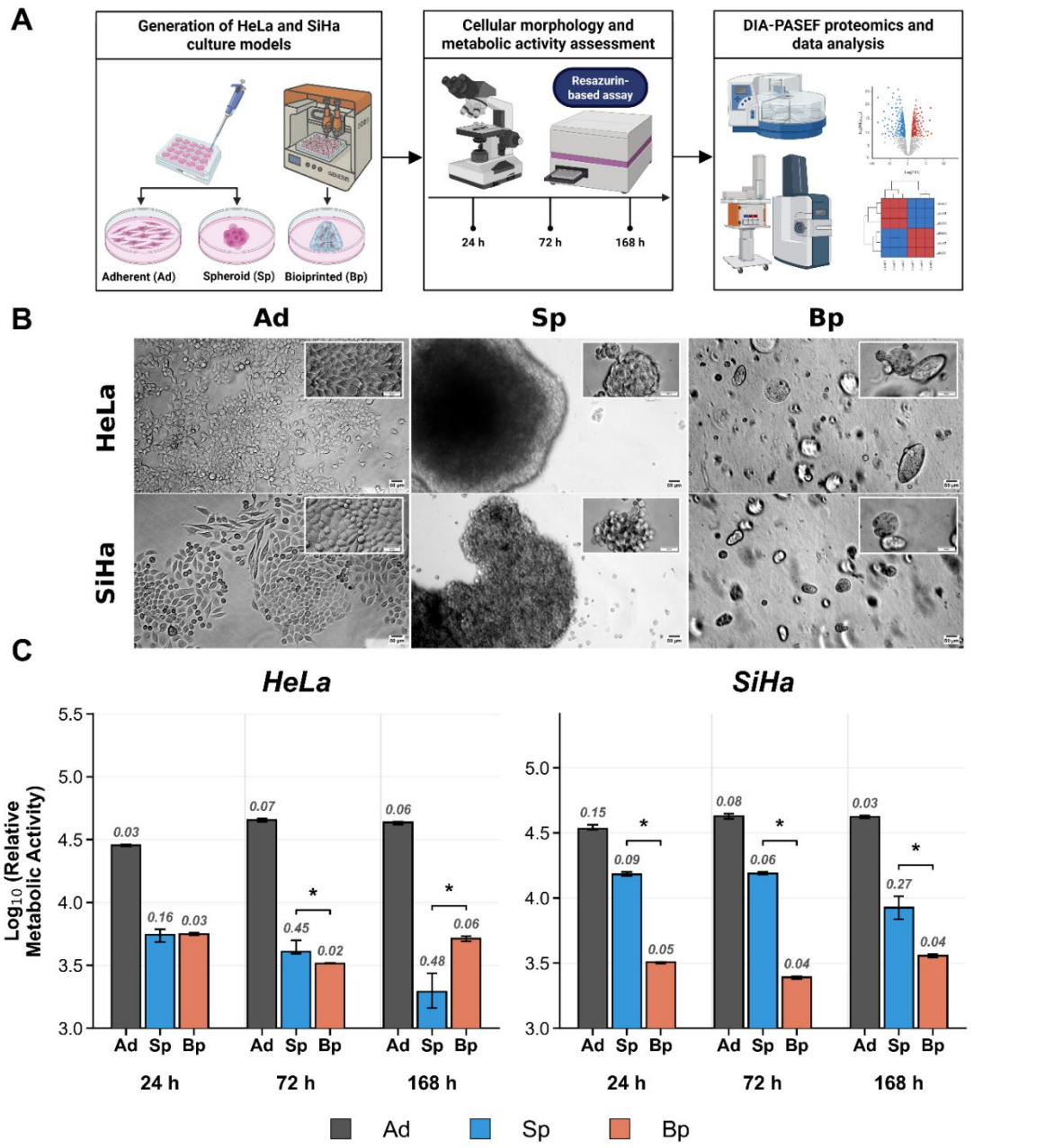


Figure 1. Morphology and relative metabolic activity of cervical cancer cells in 2D, spheroid, and bioprinted models. (A) Experimental workflow comparing HeLa and SiHa cells cultured as adherent monolayers (Ad), scaffold-free spheroids (Sp), and 3D bioprinted alginate/gelatin constructs (Bp), followed by morphological assessment, resazurin-based metabolic activity measurement, and DIA-PASEF proteomic analysis. (B) Representative bright-field images at 168 h showing architecture-dependent cellular organization. (C) Resazurin-based relative metabolic activity at 24, 72, and 168 h, shown as log10-transformed relative metabolic activity. Bars represent the median, and error bars indicate the interquartile range (IQR, 25th–75th percentiles). Numbers above bars indicate the coefficient of variation (CV). Statistical differences between spheroid (Sp) and bioprinted (Bp) models were evaluated at each time point using a two-sided Mann–Whitney U test. P-values were not adjusted for multiple comparisons. *$p < 0.05$, **$p < 0.01$, ***$p < 0.001$.

Adherent cultures formed monolayer-like distributions, with HeLa cells displaying a more dispersed epithelial-like arrangement and SiHa cells forming more compact cellular islands. Spheroids generated dense multicellular aggregates in both cell lines, although HeLa spheroids appeared more compact and showed a darker central region, whereas SiHa spheroids displayed a more irregular multicellular structure. This morphology was consistent with compact cellular packing and potentially diffusion-limited organization. In bioprinted constructs, both cell lines were embedded within the alginate/gelatin hydrogel as isolated cells and small multicellular clusters, with local differences in aggregate size and spatial distribution between HeLa and SiHa. Relative metabolic activity differed across culture systems, time points, and cell lines (Fig. 1C). In HeLa cells, adherent cultures showed a higher resazurin-based metabolic signal than both 3D models throughout the time course, with the largest separation at 168 h, when the adherent condition showed a 22.11-fold higher signal than spheroids and an 8.40-fold higher signal than bioprinted models. Direct Sp *vs* Bp comparisons were not significant at 24 h ($p = 1.0000$) but became significant at 72 h and 168 h ($p = 0.0286$ for both comparisons). At 72 h, spheroids showed a modestly higher signal than bioprinted models, whereas at 168 h, bioprinted models showed a higher signal than spheroids. SiHa cells showed a more consistent separation between the two 3D architectures. Spheroids displayed higher resazurin-based relative metabolic signal than bioprinted models at all evaluated time points, with Sp/Bp ratios of 4.73-fold at 24 h, 6.27-fold at 72 h, and 2.34-fold at 168 h. These Sp *vs* Bp differences were significant at each time point ($p = 0.0286$). Relative to adherent cultures, the reduction in metabolic signal was more pronounced in bioprinted models than in spheroids, particularly at 72 h, when the Ad/Bp ratio reached 17.29-fold. Thus, morphology and resazurin-based relative metabolic activity indicated architecture- and cell line-dependent differences before proteomic profiling.

2.2 Global proteomic profiling reveals architecture-dependent organization and consistent quantitative performance

To determine whether the morphological and metabolic differences observed across culture systems were reflected in the global proteome, we performed DIA-PASEF-based proteomic profiling at 168 h. The analysis identified 8,837 protein groups across the complete experiment, with greater identification depth in HeLa than in SiHa after cell line-level processing (Fig. 2; Supplementary Fig. S1; Supplementary Table S1).

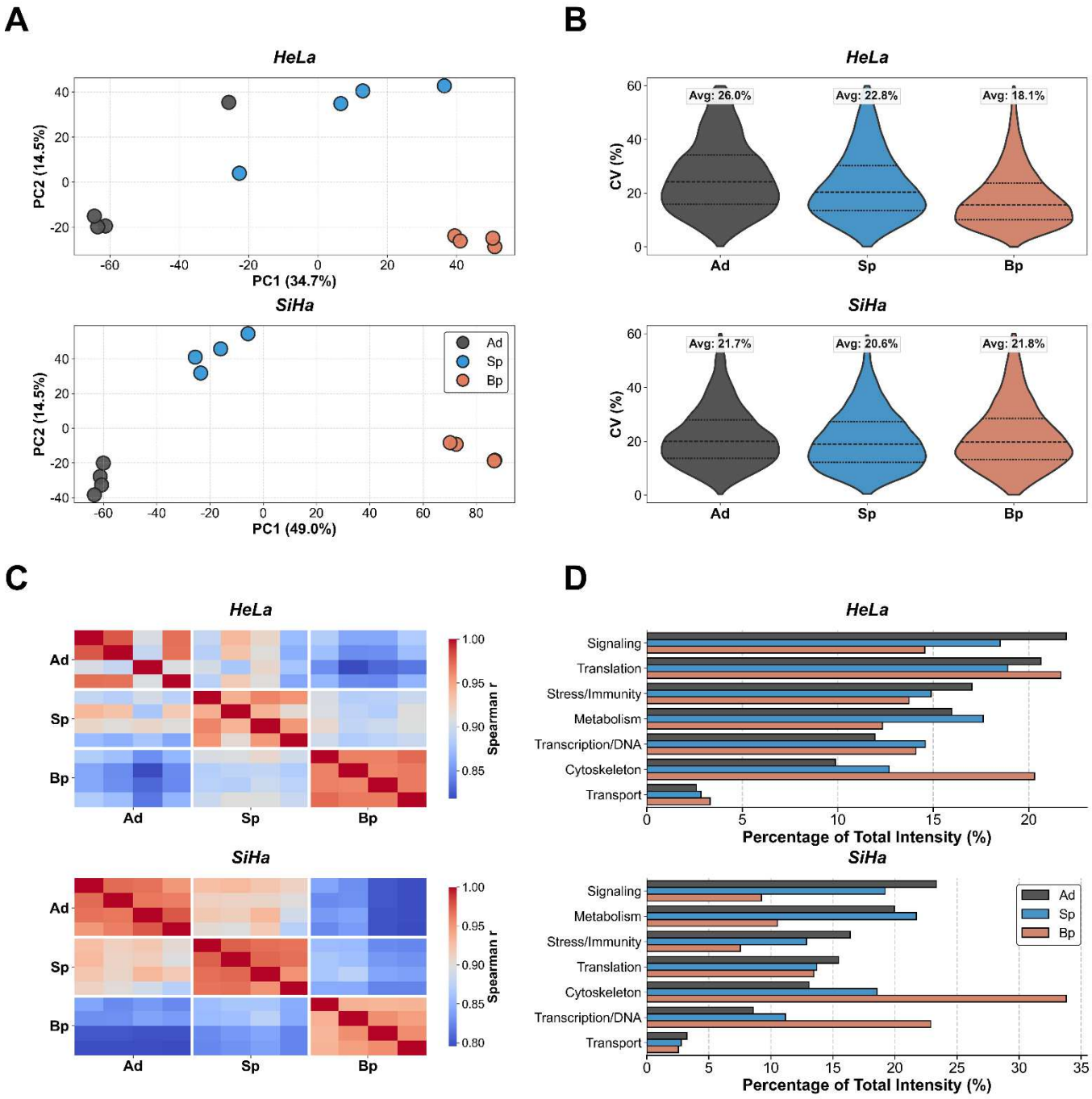


Figure 2. Global proteomic quality control and architecture-dependent sample organization. (A) Principal component analysis of protein abundance profiles from HeLa and SiHa cells cultured under Ad, Sp, and Bp conditions. (B) Distribution of protein-level coefficients of variation across culture architectures. Proteins with CV > 60% were excluded from CV visualization and average CV reporting. (C) Spearman correlation heatmaps showing replicate-level consistency. (D) Grouped horizontal bar plots showing the relative distribution of broad functional protein categories across architectures in each cell line. Additional QC metrics are provided in Supplementary Fig. S1 and Supplementary Table S1.

After cell line-specific processing, 6,496 protein groups were retained for downstream analysis in HeLa and 5,216 in SiHa. Differences in identification depth were also evident at the peptide and precursor levels. Principal component analysis showed that global proteomic variation was organized by culture architecture in both cell lines (Fig. 2A). In HeLa, Ad, Sp, and Bp samples occupied distinct regions of the PCA space, although individual Ad and Sp replicates showed moderate dispersion along PC2. Bioprinted HeLa replicates formed a compact group, consistent with the lower average CV observed for this condition. In SiHa, architecture-dependent separation was more pronounced, with Ad, Sp, and Bp forming clearer clusters across PC1 and PC2. PC1 and PC2 explained 34.7% and 14.5% of the variance in HeLa, and 49.0% and 14.5% in SiHa, respectively.

Protein-level coefficient-of-variation distributions and replicate-level correlations supported consistent quantitative performance across architectures (Fig. 2B, C). In HeLa, average CV values were 26.0% for Ad, 22.8% for Sp, and 18.1% for Bp, indicating the lowest variability in the bioprinted condition. In SiHa, average CV values were comparable across models, with 21.7% for Ad, 20.6% for Sp, and 21.8% for Bp. Spearman correlation patterns further supported within-condition consistency and architecture-dependent grouping, with clearer architecture-associated correlation blocks in SiHa and a compact Bp cluster in HeLa. These QC patterns indicate that the architecture-dependent proteomic separation was not driven by increased variability in the 3D models.

Broad functional category annotation provided a descriptive overview of the detected proteome across culture systems (Fig. 2D). In HeLa, the relative distribution of broad functional categories was generally comparable across architectures, with signaling, translation, metabolism, and stress/immunity remaining among the most represented classes in all three conditions. However, bioprinted HeLa samples showed a higher relative contribution of cytoskeleton-associated proteins compared with adherent and spheroid cultures, whereas adherent and spheroid models retained higher relative contributions from signaling- and metabolism-associated categories. In addition, translation-related proteins remained prominently represented across all HeLa architectures, while transport-associated proteins accounted for only a minor fraction of the detected proteome.

In SiHa, the grouped category profiles revealed a more pronounced architecture-dependent redistribution. Adherent and spheroid cultures retained a stronger relative representation of

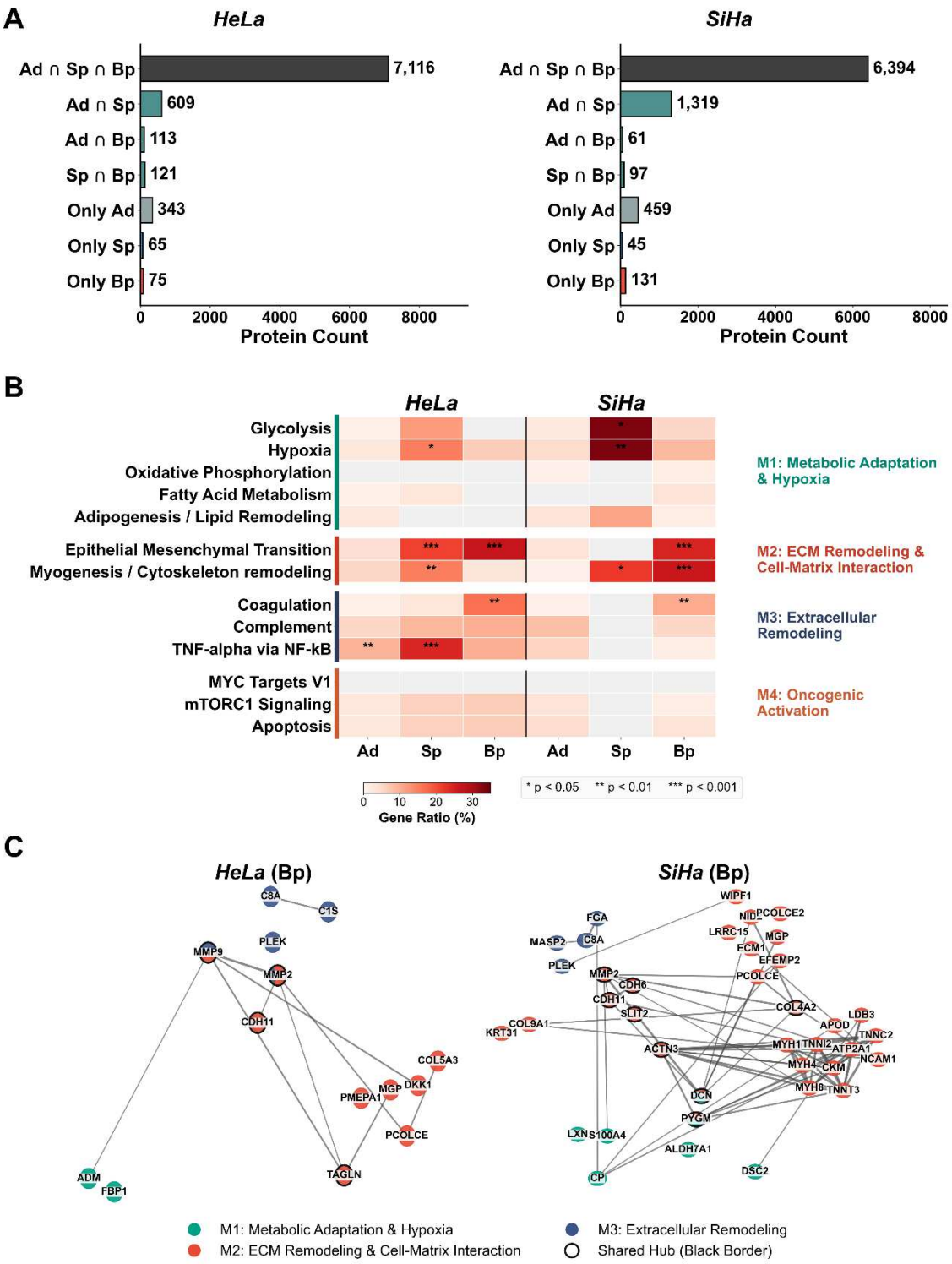
signaling, metabolism, stress/immunity, and translation-associated categories, whereas the bioprinted condition showed a marked increase in cytoskeleton-associated proteins, along with a higher relative representation of transcription/DNA-associated proteins. By contrast, metabolism- and signaling-associated categories were comparatively reduced in the SiHa bioprinted model. Overall, the grouped category profiles were consistent with the PCA, CV, and correlation analyses, supporting a robust and biologically structured dataset suitable for downstream assessment of architecture-dependent proteomic remodeling.

2.3 Architecture-associated detected protein subsets reveal model-dependent functional annotations.

Next, we asked whether each culture architecture contributed distinct subsets of proteins at the detection level before evaluating changes in quantitative abundance. This presence/absence-based analysis was performed using the non-imputed detection matrix prior to quantitative retention, imputation, and normalization; therefore, subset counts describe protein detection and are not expected to match the retained quantitative matrices used for differential abundance testing. This analysis provided a qualitative view of architecture-associated protein detection across adherent, spheroid, and bioprinted models (Fig. 3A). Most proteins were detected in all three culture systems, with 7,116 shared proteins in HeLa and 6,394 in SiHa. Smaller architecture-restricted subsets were also identified. In HeLa, 343 proteins were detected only in Ad, 65 only in Sp, and 75 only in Bp, whereas in SiHa, 459 proteins were detected only in Ad, 45 only in Sp, and 131 only in Bp. Pairwise overlaps were also architecture-dependent, with the Ad–Sp overlap exceeding the Ad–Bp and Sp–Bp overlaps in both cell lines, particularly in SiHa, where 1,319 proteins were shared between Ad and Sp, compared with 61 between Ad and Bp and 97 between Sp and Bp. Functional annotation of these detected subsets revealed architecture- and cell line-dependent enrichment patterns organized into four thematic modules (Fig. 3B; Supplementary Table S2). Module M1 comprised metabolic adaptation and hypoxia-related terms, including glycolysis, hypoxia, oxidative phosphorylation, fatty acid metabolism, and adipogenesis/lipid remodeling. Module M2 comprised ECM remodeling and cell-matrix interaction-related terms, including epithelial–mesenchymal transition and myogenesis/cytoskeleton remodeling. Module M3, designated Extracellular Remodeling, comprised Coagulation, Complement, and TNF-alpha via NF-kB annotations, whereas Module M4 grouped broader oncogenic activation-related processes, including MYC

targets V1, mTORC1 signaling, and apoptosis. Within this framework, HeLa spheroid-associated detection was linked to glycolysis and hypoxia and showed nominally significant enrichment for epithelial–mesenchymal transition, myogenesis/cytoskeleton remodeling, and TNF-alpha via NF-kB signaling. In contrast, the HeLa bioprinted-associated subset was more strongly associated with epithelial–mesenchymal transition, with coagulation also represented among the enriched annotations. In SiHa, the strongest enrichment patterns were concentrated in the spheroid and bioprinted subsets. The spheroid-associated subset showed nominally significant enrichment for glycolysis, hypoxia, and myogenesis/cytoskeleton remodeling, whereas the bioprinted-associated subset was dominated by epithelial–mesenchymal transition and myogenesis/cytoskeleton remodeling, with coagulation also represented among the enriched annotations. Across both cell lines, module M4 terms showed weaker or absent subset-specific enrichment.

STRING protein association networks further supported architecture-associated organization among the bioprinted-detected proteins (Fig. 3C). In HeLa, the Bp-associated network was composed of a relatively compact ECM/cell-matrix remodeling cluster that included MMP9, MMP2, CDH11, TAGLN, PMEPA1, MGP, DKK1, COL5A3, and PCOLCE, together with a smaller M3 group containing C8A, C1S, and PLEK, and a separate metabolic adaptation/hypoxia-related branch represented by ADM and FBP1. In SiHa, the Bp-associated network was larger and more interconnected, incorporating ECM and adhesion-related proteins such as NID2, LRRC15, ECM1, EFEMP2, PCOLCE, PCOLCE2, COL4A2, COL9A1, and KRT31, together with structural and contractile proteins including ACTN3, MYH1, MYH4, MYH8, CKM, TNNI2, TNNC2, TNNT3, ATP2A1, and NCAM1. This network also contained M3 nodes including FGA, C8A, MASP2, and PLEK, as well as a smaller group of metabolic adaptation/hypoxia-related proteins, including LXN, S100A4, ALDH7A1, CP, and DSC2. Shared hub nodes, highlighted by black borders, connected these functional modules, supporting a more integrated bioprinting-associated network in SiHa than in HeLa. Overall, this qualitative detection layer indicated that each architecture contributed distinct subsets of proteins and functional annotations to the global proteomic landscape.



245 **Figure 3. Architecture-associated detected protein subsets and functional annotations.** (A) Summary of proteins
246 detected across Ad, Sp, and Bp models in HeLa and SiHa cells using the non-imputed detection matrix. Bars indicate
247 proteins shared among all three architectures, shared between pairs of architectures, or uniquely detected in a single
248 architecture. (B) Over-representation analysis of architecture-associated detected protein subsets across Ad, Sp, and
249 Bp conditions in HeLa and SiHa cells. Hallmark terms are grouped into four thematic modules: M1, metabolic

adaptation and hypoxia; M2, ECM remodeling and cell-matrix interaction; M3, Extracellular Remodeling; and M4, oncogenic activation. Color intensity indicates gene ratio (%), and asterisks denote nominal, unadjusted p-value thresholds: *p < 0.05, **p < 0.01, and ***p < 0.001. (C) STRING protein association networks of bioprinted-associated detected proteins in HeLa and SiHa. Node colors indicate manually curated functional modules corresponding to M1, metabolic adaptation and hypoxia; M2, ECM remodeling and cell-matrix interaction; and M3, Extracellular Remodeling. Nodes with black borders indicate shared hub proteins.

2.4 Spheroid and bioprinted models diverge from adherent cultures through distinct proteomic patterns.

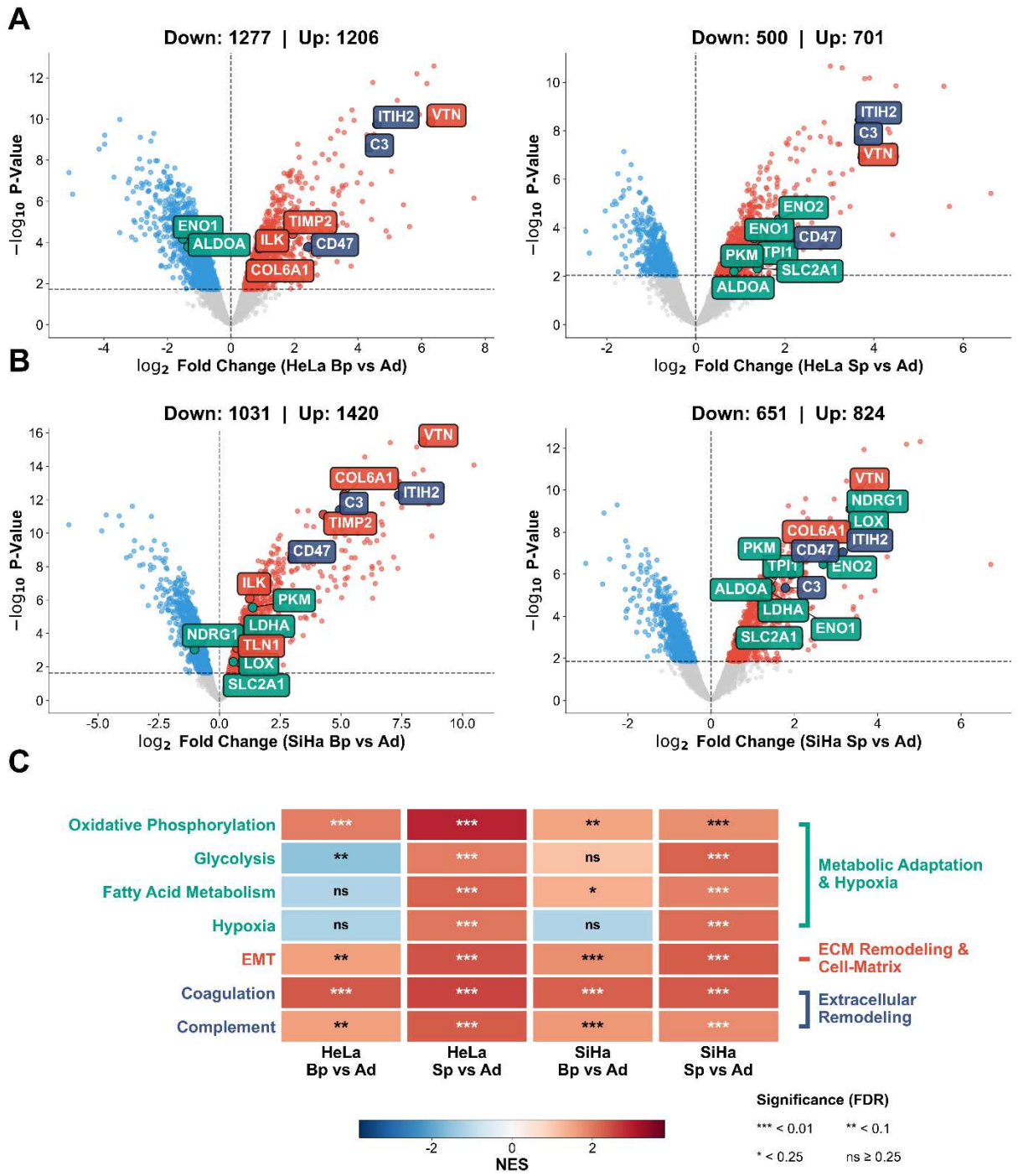
Having identified architecture-associated detection patterns, we next asked whether spheroid and bioprinted models also differed from adherent cultures in protein abundance. Quantitative differential abundance analysis was performed separately within each cell line, comparing each 3D model against its matched adherent condition (Fig. 4A, B; Supplementary Fig. S2; Supplementary Tables S3 and S4). Compared with adherent cultures, bioprinted models showed more differentially abundant proteins than spheroids in both cell lines. In HeLa, the Bp *vs* Ad comparison identified 2,483 differentially abundant proteins, including 1,277 downregulated and 1,206 upregulated proteins, whereas Sp *vs* Ad identified 1,201 differentially abundant proteins, including 500 downregulated and 701 upregulated proteins. In SiHa, Bp *vs* Ad identified 2,451 differentially abundant proteins, including 1,031 downregulated and 1,420 upregulated proteins, whereas Sp *vs* Ad identified 1,475 differentially abundant proteins, including 651 downregulated and 824 upregulated proteins. The direction and identity of highlighted proteins suggested partially distinct architecture-associated proteomic states. Spheroid comparisons were preferentially characterized by increased abundance of metabolic and hypoxia-associated proteins, including glycolytic enzymes and stress-related proteins such as ENO1, ENO2, TPI1, PKM, SLC2A1, LDHA, ALDOA, NDRG1, and LOX. Bioprinted comparisons showed greater representation of highlighted ECM remodeling and cell-matrix-associated proteins, including VTN, TIMP2, ILK, TLN1, and COL6A1, together with selected extracellular-remodeling proteins such as ITIH2, C3, and CD47 (Fig. 4A, B). This pattern was particularly evident in SiHa Bp *vs* Ad, where selected ECM/cell-matrix and extracellular-remodeling proteins showed strong positive shifts.

Hallmark fGSEA was summarized as an NES heatmap to evaluate whether these protein-level patterns were reflected at the pathway-signature level (Fig. 4C; Table 2). Spheroid models showed more consistent representation of metabolic and hypoxia-associated Hallmarks. Glycolysis and

hypoxia-associated terms displayed positive NES values with FDR support in both HeLa Sp *vs* Ad and SiHa Sp *vs* Ad, whereas these terms were weaker, negative, or not FDR-supported in the bioprinted comparisons. Fatty acid metabolism also showed stronger positive representation in spheroid comparisons, particularly in HeLa Sp *vs* Ad and SiHa Sp *vs* Ad. Oxidative phosphorylation showed positive NES values across all 3D *vs* adherent comparisons, indicating that energy metabolism was broadly remodeled in 3D culture rather than restricted to a single architecture.

ECM/cell-matrix and extracellular-remodeling signatures were also represented across 3D *vs* adherent comparisons. EMT showed positive NES values in all four contrasts, with FDR-supported enrichment in both spheroid and bioprinted models. Coagulation and complement also showed positive NES values across the four 3D *vs* adherent comparisons. Therefore, these annotations were not interpreted as exclusively associated with bioprinting at this stage. Instead, the 3D *vs* adherent analysis indicated that ECM/cell-matrix and extracellular-remodeling signatures contributed to a broader 3D-associated response, while selected protein-level patterns were more prominently represented in bioprinted models, particularly in SiHa.

Extended GO Biological Process analysis supported the same module-level organization, with metabolic and respiration-related terms represented among spheroid-associated comparisons and ECM organization, glycoprotein metabolism, cell adhesion, hemostasis, wound healing, and humoral immune response annotations contributing to the broader 3D-associated remodeling signature (Supplementary Fig. S3; Supplementary Table S4). Together, these results showed that both spheroid and bioprinted models diverged from adherent cultures, but that a direct Bp *vs* Sp analysis was required to distinguish which components were preferentially associated with each 3D architecture.



304 **Figure 4. Differential proteomic remodeling of spheroid and bioprinted models relative to adherent cultures. (A)**
305 **Volcano plots showing differential protein abundance in HeLa Bp *vs* Ad and HeLa Sp *vs* Ad comparisons.** (B) Volcano
306 plots showing differential protein abundance in SiHa Bp *vs* Ad and SiHa Sp *vs* Ad comparisons. Differentially
307 abundant proteins were defined using FDR < 0.05. Representative proteins from the metabolic adaptation/hypoxia,
308 ECM remodeling/cell-matrix interaction, and extracellular remodeling categories are highlighted. (C) Hallmark
309 fGSEA NES heatmap across 3D *vs* adherent comparisons. Color indicates normalized enrichment score (NES), and
310 asterisks indicate FDR thresholds: ***FDR < 0.01, **FDR < 0.1, *FDR < 0.25, and ns FDR ≥ 0.25.

2.5 Direct Bp *vs* Sp comparison identifies non-interchangeable 3D proteomic states.

Because spheroid and bioprinted models both diverged from adherent cultures yet showed partially distinct proteomic signatures, we next directly compared the two 3D architectures. The Bp *vs* Sp contrast revealed extensive proteomic divergence between spheroid and bioprinted models in both cell lines (Fig. 5A; Supplementary Table S3). In HeLa cells, the FDR-defined comparison identified 1,332 differentially abundant proteins, including 535 Bp-high and 797 Sp-high proteins. In SiHa cells, the same comparison identified 2,212 differentially abundant proteins, including 1,311 Bp-high and 901 Sp-high proteins. The architecture-skewed protein pattern was partially concordant across cell lines. Spheroid-high proteins were dominated by metabolic and hypoxia-associated features, including ENO1, ENO2, TPI1, PGAM1, ALDOA, LDHA, NDRG1, LOX, and P4HA1. Bioprinted-high proteins highlighted in one or both cell lines included ECM remodeling and cell-matrix-associated proteins such as VTN, TIMP2, ILK, and COL6A1, together with selected extracellular-remodeling proteins including ITIH2, C3, and CD47 (Fig. 5A, Table 1).

To assess whether these architecture-skewed differences were conserved across cell lines, we compared direct Bp *vs* Sp log2 fold-changes between HeLa and SiHa (Fig. 5B). The overall relationship was positive ($r = 0.537$), indicating a shared direction of 3D architectural remodeling. Several metabolic and hypoxia-associated proteins clustered in the lower-left quadrant, consistent with higher abundance in spheroids in both cell lines, whereas selected ECM/cell-matrix and extracellular-remodeling proteins occupied the upper-right quadrant, consistent with higher abundance in bioprinted models. This pattern was especially evident for ENO1, ENO2, PGAM1, ALDOA, TPI1, and LDHA on the spheroid-associated side, and for VTN, TIMP2, COL6A1, C3, and ITIH2 on the bioprinted-associated side (Fig. 5B).

Pathway-level analysis further supported this direct 3D-to-3D divergence (Fig. 5C; Supplementary Fig. S3; Supplementary Table S4). In both cell lines, spheroid-associated profiles showed negative NES values for oxidative phosphorylation, glycolysis, fatty acid metabolism, and hypoxia, although oxidative phosphorylation and fatty acid metabolism did not meet the displayed FDR threshold in SiHa. Coagulation showed a positive NES in SiHa Bp *vs* Sp (FDR < 0.01), but a negative, non-significant NES in HeLa. Complement showed negative NES values in both cell lines (FDR < 0.1), whereas EMT displayed a negative NES in HeLa (FDR < 0.1) and a positive NES in SiHa that did not meet the displayed FDR threshold. Extended GO Biological Process

analysis supported the same overall separation, with spheroid-prominent metabolic processes and bioprinted-prominent terms such as adhesion, glycoprotein metabolism, hemostasis, and humoral immune response (Supplementary Fig. S3). Together, these direct Bp *vs* Sp comparisons establish that spheroid and bioprinted cultures produce distinct proteomic states rather than interchangeable alternatives to adherent culture.

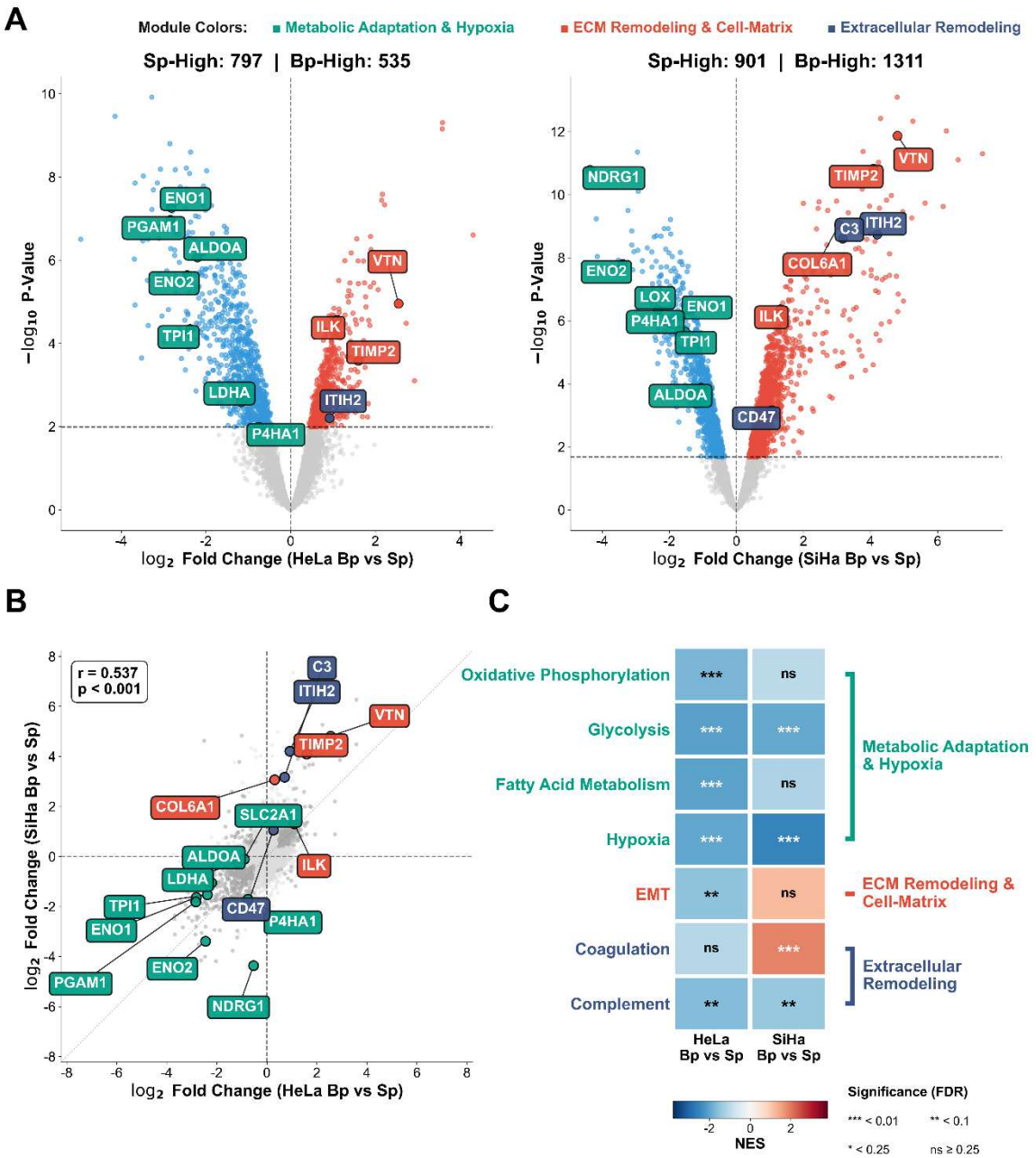


Figure 5. Direct comparison of bioprinted and spheroid models identifies distinct 3D proteomic states. (A) Volcano plots showing direct Bp *vs* Sp differential protein abundance in HeLa and SiHa cells. Positive log2 fold-change values indicate higher abundance in Bp, whereas negative values indicate higher abundance in

Sp. Differentially abundant proteins were defined using FDR < 0.05. Representative proteins from the metabolic adaptation/hypoxia, ECM remodeling/cell-matrix interaction, and extracellular remodeling categories are highlighted. (B) Cross-cell-line comparison of direct Bp *vs* Sp log2 fold-changes in HeLa and SiHa cells (Spearman r = 0.537). Proteins in the upper-right and lower-left quadrants show concordant architectural skewing across both cell lines. (C) Hallmark-based pathway summary of the direct Bp *vs* Sp comparison. Tile color represents the normalized enrichment score (NES), and in-cell labels indicate FDR thresholds: ***FDR < 0.01, **FDR < 0.1, *FDR < 0.25, and ns FDR ≥ 0.25. Extended GO Biological Process analysis is provided in Supplementary Fig. S3.

2.6 Selected protein-level assessment recapitulates architecture-associated modules.

Finally, we examined selected proteins representing the main modules identified in the global analyses to determine whether the architecture-associated patterns were also evident at the individual-protein level (Fig. 6; Supplementary Table S5). The selected metabolic proteins recapitulated a predominantly spheroid-skewed profile. In HeLa, ENO2 and ENO1 increased significantly in spheroids relative to adherent cultures and decreased in bioprinted models, while TPI1 showed the same directionality. SLC2A1 and PKM showed higher mean abundance in spheroids, but these changes were less pronounced. In SiHa, ENO2, ENO1, and TPI1 increased in spheroids, whereas SLC2A1 and PKM increased in both 3D architectures, indicating that part of the metabolic shift was shared between spheroid and bioprinted SiHa models. The selected ECM remodeling and cell-matrix-associated proteins showed a stronger bioprinting-associated profile (Fig. 6). TLN1 showed higher mean abundance in bioprinted SiHa cells, whereas its abundance remained comparatively stable across architectures in HeLa. TIMP2 and ILK showed larger abundance increases in Bp than in Sp relative to Ad. This pattern was particularly evident in SiHa, where TIMP2, ILK, and TLN1 showed marked Bp-associated increases. Selected extracellular-remodeling proteins also showed architecture-associated abundance differences in both cell lines (Fig. 6). C3, CD47, and ITIH2 showed their highest mean abundance in bioprinted models in both cell lines, whereas CLU was highest in spheroids. In HeLa, C3, CD47, and ITIH2 also showed higher abundance in spheroids relative to adherent cultures, although bioprinted models displayed the highest mean values. In SiHa, Bp-associated abundance increases were particularly pronounced for C3 and ITIH2, whereas CLU retained a spheroid-high profile.

Overall, the morphological, metabolic, global proteomic, direct 3D-to-3D, and selected protein-level analyses converged on the same architecture-dependent pattern: scaffold-free spheroids were associated with stronger metabolic and hypoxia-associated features, whereas hydrogel-supported bioprinted models displayed stronger ECM/cell-matrix and selected extracellular-remodeling protein abundance patterns.

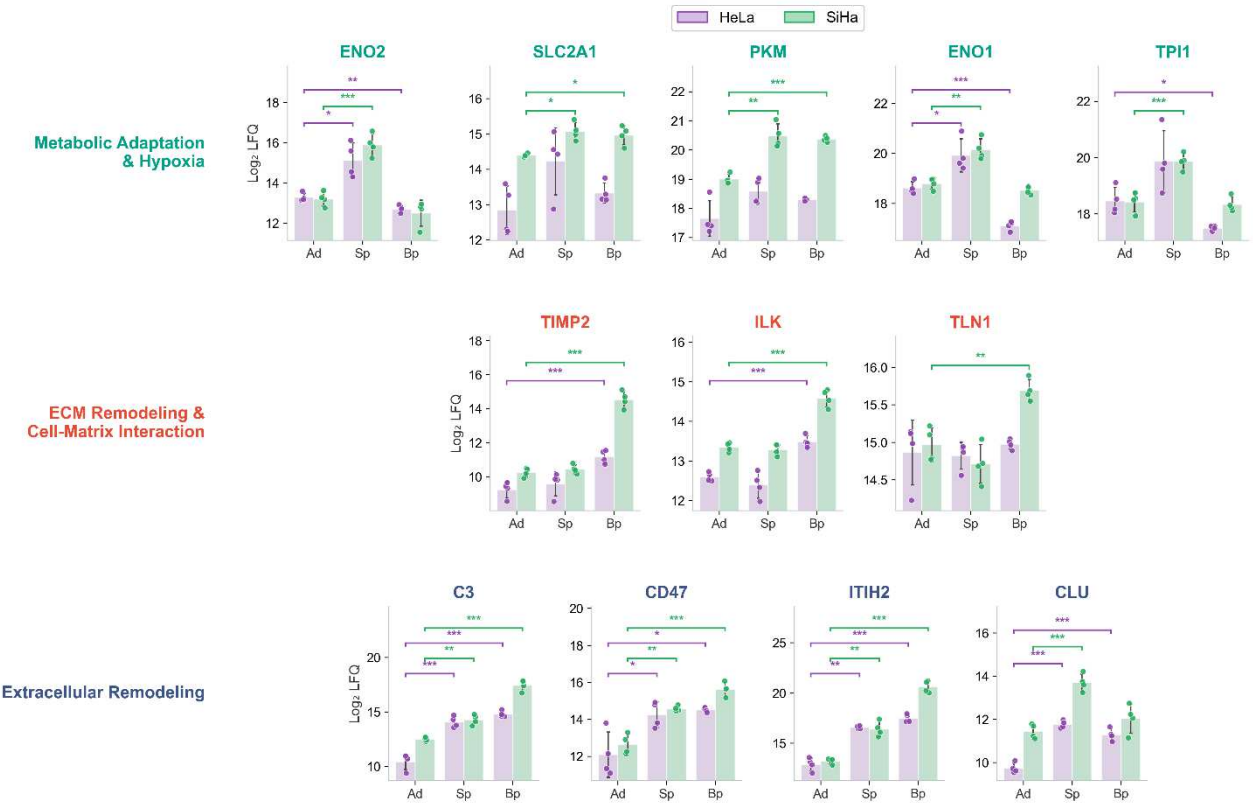


Figure 6. Selected protein-level assessment of architecture-associated modules. Normalized log2 LFQ values for 12 selected proteins representing metabolic adaptation and hypoxia, ECM remodeling and cell-matrix interaction, and extracellular remodeling. HeLa is shown in purple and SiHa in green. Each point represents an independently cultured and processed well (n = 4 per condition), and bars indicate the mean ± SD. Within each cell line, Sp *vs* Ad and Bp *vs* Ad comparisons were evaluated using Welch's t-test. *p < 0.05, **p < 0.01, ***p < 0.001. P-values are unadjusted and are presented for descriptive purposes. Complete values and statistics are provided in Supplementary Table S5.

3 Discussion

This study shows that three-dimensional culture architecture is a major determinant of the morphological, metabolic, and proteomic state of cervical cancer cells. By comparing HeLa and SiHa cells grown as adherent monolayers, scaffold-free spheroids, and 3D bioprinted alginate/gelatin constructs, we found that spheroid and bioprinted models are not interchangeable 3D systems. Instead, each architecture promoted a distinct proteomic state. Spheroids were more strongly associated with metabolic adaptation, glycolytic remodeling, and hypoxia-associated signatures, whereas bioprinted models showed a stronger representation of matrix-associated remodeling and cell-matrix interaction features. Selected extracellular-remodeling proteins emerged as part of a broader 3D-associated profile, with several showing greater representation in bioprinted models and CLU displaying a spheroid-high abundance pattern. These findings indicate that the physical and hydrogel-supported context in which cervical cancer cells are cultured can reshape the global proteomic landscape and should be considered a central experimental variable in preclinical model design.

The morphological and metabolic differences observed across culture systems provided an important phenotypic framework for interpreting the proteomic results. Adherent cultures formed conventional monolayer-like distributions and exhibited the highest metabolic signal, whereas spheroids formed compact multicellular aggregates, and bioprinted models produced hydrogel-embedded cellular structures. These differences are consistent with the broader view that 3D culture systems alter cell organization, cell–cell contact, diffusion geometry, and access to nutrients, oxygen, and soluble reagents compared with conventional monolayers [9–12]. Accordingly, the lower signal observed in 3D systems relative to adherent cultures may reflect combined effects of reagent diffusion, cellular density, nutrient availability, oxygen exposure, and metabolic state. The resazurin-based metabolic assay should therefore be interpreted as a relative readout of metabolic reducing activity rather than as a direct measurement of cell number or absolute viability. The distinct temporal trajectories observed between spheroid and bioprinted conditions further support the notion that different 3D architectures impose different physical and biochemical constraints on cervical cancer cells.

The spheroid-high proteomic profile was dominated by proteins associated with glycolysis and hypoxia-associated remodeling, including ENO1, ENO2, TPI1, PGAM1, ALDOA, LDHA,

NDRG1, LOX, P4HA1, and SLC2A1/GLUT1. This pattern is consistent with the established capacity of compact multicellular tumor spheroids to generate architecture-dependent gradients in oxygen, glucose, extracellular pH, and metabolites, leading to spatially heterogeneous metabolic states [13,15,30]. Previous tumor spheroid studies have also shown that multicellular organization can reshape energy metabolism and promote glycolytic adaptation [13,31]. More specifically, HeLa spheroid studies have linked spheroid architecture with glucose diffusion constraints, glycolytic oscillations, and altered energy metabolism [16,17]. In this context, the increased abundance of glycolytic enzymes and hypoxia-associated markers in spheroids supports an architecture-associated metabolic remodeling phenotype compatible with diffusion-limited adaptation. Because oxygen tension, HIF-1α stabilization, HIF transcriptional activity, and hypoxia-specific staining were not directly assessed, these results should be interpreted as hypoxia-associated rather than as direct evidence of hypoxia or HIF-1 pathway activation.

In contrast to scaffold-free spheroids, the alginate/gelatin bioprinted constructs provided a hydrogel-supported 3D context in which tumor cells were embedded within a defined architecture. This distinction is relevant because previous cervical cancer bioprinting studies using HeLa cells and gelatin/alginate-containing bioinks have shown that 3D-printed models differ from 2D monolayers in cellular organization, extracellular remodeling-associated proteins, EMT-related responses, proliferation, and chemoresistance [21–24]. Additional studies of hydrogel-supported tumor models indicate that alginate/gelatin-based scaffolds and related bioinks can influence tumor cell organization, matrix-associated remodeling, and drug response [18–20]. Consistent with this framework, our bioprinted models showed increased abundance of matrix- and cell-matrix-associated proteins, including VTN, TIMP2, ILK, TLN1, and COL6A1. These changes support a scaffold-associated matrix-remodeling and cell-matrix-interaction signature. Because the model contains only cervical cancer cells embedded in an alginate/gelatin hydrogel and lacks fibroblasts, endothelial cells, immune cells, and native stromal ECM, these findings are best interpreted as tumor-cell responses to a hydrogel-supported architecture rather than as a complete recapitulation of the tumor microenvironment.

Higher ILK abundance in bioprinted models reinforced the interpretation of a cell-matrix interaction profile within the scaffolded 3D context. ILK is an integrin-linked focal adhesion-associated protein that participates in adhesion complex organization and connects integrin engagement with actin-associated remodeling through the ILK–PINCH–parvin complex [32–35].

In cancer models, ILK has also been associated with adhesion-linked invasion, ECM proteolysis, EMT-related behavior, and metastatic phenotypes [36,37]. In our dataset, increased ILK abundance is therefore consistent with an adhesion-linked, cell-matrix interaction profile associated with the bioprinted architecture. This interpretation remains at the protein-abundance level and should not be taken as direct evidence of mechanotransduction activation, which would require functional assessment of kinase activity, phosphorylation status, traction forces, or nuclear mechanotransduction effectors.

Selected extracellular-remodeling proteins, including C3, CD47, ITIH2, and CLU, also showed architecture-associated abundance differences in both cell lines. At the pathway level, coagulation and complement-associated terms were represented across 3D contrasts, suggesting that this signature reflects a broader 3D-associated remodeling profile rather than an exclusively bioprinted-specific response. Nevertheless, direct Bp *vs* Sp comparisons and selected protein-level patterns indicated higher Bp-associated abundance for several extracellular-remodeling proteins, particularly in SiHa, while CLU showed a spheroid-high profile. Coagulation-associated processes have been linked to cancer progression and metastasis [38–40]. Given the absence of immune cells, endothelial cells, stromal cells, blood, and plasma in this system, these findings should be interpreted at the protein-abundance level rather than as evidence of functional immune activation, vascular activation, complement cascade activation, or coagulation cascade activation.

The direct comparison between bioprinted and spheroid models was central to defining the biological meaning of these architecture-dependent changes. Comparisons against adherent monolayers showed that both 3D systems were extensively remodeled relative to 2D culture. However, the direct Bp *vs* Sp analysis demonstrated that the two 3D models diverged from each other rather than representing equivalent alternatives to adherent culture. Spheroids preferentially retained a glycolytic and hypoxia-associated protein profile, whereas bioprinted models showed higher abundance of selected ECM/cell-matrix and extracellular-remodeling proteins. The cross-cell-line Bp *vs* Sp comparison further indicated partial concordance between HeLa and SiHa, with several metabolic/hypoxia-associated proteins displaying spheroid-high abundance and selected ECM/cell-matrix and extracellular-remodeling proteins displaying bioprinted-high abundance in both cell lines. This distinction prevents overclassifying these proteins as strictly bioprinting-specific while supporting the conclusion that bioprinted models occupy a proteomic state distinct from that of spheroids.

These findings have practical implications for cervical cancer model selection. Spheroids may be particularly useful for studying compact tumor growth, diffusion-limited architecture, hypoxia-associated metabolic adaptation, glycolytic remodeling, and experimental contexts related to metabolic stress. Bioprinted alginate/gelatin models, by contrast, may be more suitable for investigating scaffold-associated matrix remodeling, cell-matrix interaction, adhesion-linked profiles, and selected tumor-cell-associated extracellular remodeling features. Therefore, the choice of 3D model should be guided by the biological question being addressed rather than by the general use of three-dimensionality as a single experimental category.

The study also highlights the value of DIA-PASEF proteomics for benchmarking *in vitro* tumor models. Morphology and metabolic activity assays are useful for initial phenotypic characterization, but they provide limited information about the molecular state induced by each architecture. By integrating label-free quantitative proteomics with differential protein analysis, pathway enrichment, direct 3D-to-3D comparison, and selected protein-level assessment, we identified architecture-dependent molecular patterns that would not be evident from morphology or metabolic activity alone, linking spheroid-associated metabolic/glycolytic remodeling with bioprinted ECM/cell-matrix and selected extracellular-remodeling protein profiles. This approach can support more rational benchmarking of 3D cancer models and may help define which experimental systems are most appropriate for specific mechanistic or translational applications.

Several limitations should be considered when interpreting these findings. The use of established cervical cancer cell lines does not capture the full heterogeneity of patient-derived tumors, and the alginate/gelatin formulation represents one specific hydrogel context among many possible scaffold designs. The observed proteomic state may therefore vary with tumor origin, scaffold composition, crosslinking, stiffness, porosity, and hydrogel-associated protein retention. In addition, the study focused on global protein abundance rather than post-translational regulation, mechanical forces, oxygen gradients, or spatial protein distribution. Accordingly, pathway-level annotations related to hypoxia-associated terms, focal adhesion signaling, mechanotransduction, complement, or coagulation should be interpreted as associated signatures rather than mechanistically demonstrated pathway activation. Finally, the resazurin-based metabolic assay reflects relative metabolic reducing activity and reagent accessibility and should not be interpreted as a direct measure of cell number without complementary assays.

Future studies should extend this framework using patient-derived cervical cancer organoids, primary tumor cells, stromal or immune-containing co-cultures, and bioinks with controlled mechanical and biochemical properties. Spatially resolved approaches, including oxygen-sensitive probes, imaging-based protein analysis, or spatial proteomics, would help determine how metabolic and proteomic states are distributed within 3D constructs. Complementary phosphoproteomic, mechanical, and drug-response assays could further clarify whether the architecture-dependent molecular states identified here translate into functional signaling differences or therapeutic vulnerabilities.

In conclusion, our data demonstrate that 3D architecture strongly reshapes the proteomic landscape of cervical cancer cells. Spheroids and bioprinted alginate/gelatin models both differ from adherent monolayers, but in distinct ways. Spheroids preferentially exhibited glycolytic remodeling and hypoxia-associated metabolic signatures, whereas bioprinted models showed stronger matrix-associated and cell-matrix interaction profiles. Coagulation/complement-associated proteins appear as part of a broader 3D-associated remodeling profile, with selected components showing stronger representation in bioprinted models. These findings support using proteomics as a framework for benchmarking 3D cancer models and emphasize that culture architecture should be selected based on the biological process under investigation.

4 Methods

4.1 Experimental design

This study was designed as a systematic comparison between conventional adherent monolayers, scaffold-free spheroids, and 3D bioprinted alginate/gelatin models of cervical cancer. Human HeLa and SiHa cervical cancer cell lines were cultured under three architectural conditions: adherent monolayers (Ad), spheroids (Sp), and bioprinted constructs (Bp). Morphology and resazurin-based relative metabolic activity were assessed over time, and DIA-PASEF-based global proteomic profiling was performed at 168 h. The resulting protein abundance data were analyzed using quality-control metrics, architecture-associated detected-protein subset analysis, differential protein abundance testing, pathway-level enrichment, protein association networks, and selected protein-level assessments.

4.2 Cell culture

Human cervical cancer HeLa and SiHa cell lines were obtained from the American Type Culture Collection (ATCC, USA). Cells were maintained in Dulbecco's modified Eagle medium (DMEM) supplemented with 10% fetal bovine serum and 1% penicillin–streptomycin. Cultures were incubated at 37 °C in a humidified atmosphere containing 5% CO_2. Cells were routinely passaged using 0.25% trypsin–EDTA and maintained under sterile culture conditions. Culture medium was replaced every 48 h during the experimental period.

4.3 Generation of adherent, spheroid, and bioprinted models

For each cell line, three culture architectures were established: adherent monolayers (Ad), scaffold-free spheroids (Sp), and 3D bioprinted alginate/gelatin constructs (Bp). Adherent cultures were seeded in standard tissue culture plates and maintained under conventional monolayer conditions. Spheroids were generated in agarose-coated 24-well plates. Briefly, wells were coated with 300 µL of sterile 1% agarose prepared in phosphate-buffered saline (PBS), and 2,000 cells were seeded per well to promote scaffold-free multicellular aggregation. Bioprinted constructs were generated using an alginate/gelatin bioink prepared at 3% alginate and 7% gelatin (w/v) in sterile PBS. For a 30 mL preparation, 900 mg alginate and 2,100 mg gelatin type A (Merck) were dissolved in PBS supplemented with 500 µL penicillin–streptomycin and 10 µL fungin. The bioink was sterilized by UV exposure and filtration through a 0.45 µm membrane before use. Cells were mixed with the bioink to generate constructs containing 2,000 cells per printed dome. Bioprinting was performed using a Genesis bioprinter (3D Biotechnology Solutions) equipped with a 23G needle. Each construct consisted of a 60 µL dome printed in a 24-well plate. After printing, constructs were crosslinked with 400 µL of 50 mM $CaCl_2$ (Merck) for 5 min at room temperature, washed with 500 µL warm Hank's balanced salt solution (HBSS), and maintained in 500 µL complete DMEM. All models were cultured for up to 168 h.

4.4 Morphological assessment and relative metabolic activity

Cellular morphology was evaluated by bright-field microscopy at the indicated time points. Representative images were acquired to document architecture-dependent organization in adherent, spheroid, and bioprinted cultures. Relative metabolic activity was assessed using a

resazurin-based assay (Alamar Blue reagent, Thermo Fisher Scientific) at 24, 72, and 168 h. The reagent was added to the culture medium at 10% of the final volume, and cells were incubated for 6 h at 37 °C. Fluorescence was measured using excitation and emission wavelengths of 530 and 590 nm, respectively. Background-corrected relative fluorescence units (RFU) were log10-transformed for visualization. Four independently cultured wells were analyzed per condition at each time point (n = 4). Spheroid and bioprinted conditions were compared at each time point using the Mann–Whitney U test. Results were visualized as medians and interquartile ranges, and coefficients of variation were calculated as the standard deviation divided by the mean.

4.5 Protein extraction

Protein extraction was performed after 168 h of culture. Before lysis, cells were recovered from each culture architecture using model-specific procedures. Adherent cells were detached with one culture volume of 0.25% trypsin–EDTA for 5 min at 37 °C, followed by enzyme inactivation with three volumes of complete DMEM, consisting of DMEM supplemented with 10% fetal bovine serum and 1% penicillin–streptomycin. Spheroids were collected by gentle pipetting without enzymatic dissociation. Bioprinted constructs were processed to release cells from the alginate/gelatin hydrogel by removing the culture medium and incubating the constructs with 5 volumes of prewarmed de-crosslinking buffer (50 mM citrate, 0.4 mM EDTA, pH 7.3) for 5 min at 37 °C. The de-crosslinking buffer was then diluted with an equal volume of prewarmed HBSS. After recovery, all samples were centrifuged at 150 × g for 5 min at 25 °C, and the resulting pellets were washed three times with prewarmed HBSS before lysis. Samples were lysed in buffer containing 100 mM Tris-HCl pH 8.5, 1% SDS, 1 mM EDTA, 75 mM NaCl, 1 mM PMSF, and protease/phosphatase inhibitors. Samples were sonicated using a Bioruptor system with 30 s on/off cycles for 10 cycles and centrifuged at 16,000 × g for 10 min at 4 °C. The supernatant was recovered, and protein concentration was determined using the Qubit protein assay (Thermo Fisher Scientific).

4.6 Protein digestion and peptide preparation

Proteins were processed using an automated SP3-based sample preparation workflow on a KingFisher Flex platform (Thermo Fisher Scientific), based on paramagnetic bead-assisted protein cleanup [27]. SP3 magnetic beads (Cytiva) were used for protein binding and cleanup. For each

sample, 30 µg of total protein was used as input. Proteins were reduced for 30 min at 60 °C and alkylated before binding to SP3 beads at a 10:1 bead-to-protein ratio. Samples were washed to remove detergents and other contaminants, and proteins were digested overnight with trypsin/LysC (Promega) at a 1:25 enzyme-to-protein ratio in 50 mM triethylammonium bicarbonate (TEAB; Merck), pH 8.5. Digestion was stopped by acidification with formic acid to a final concentration of 0.5%. Peptides were dried, resuspended in 0.1% formic acid, quantified using a NanoDrop spectrophotometer (Thermo Fisher Scientific), and stored at -80 °C until LC-MS/MS analysis.

4.7 LC-MS/MS analysis

Peptides were loaded onto C18 Evotips (Evosep Biosystems) and analyzed using an Evosep One liquid chromatography system (Evosep Biosystems) coupled to a timsTOF Pro 2 mass spectrometer equipped with a CaptiveSpray ion source (Bruker Daltonics). Peptide separation was performed using an EVOSEP Performance column (15 cm × 150 µm, 1.5 µm ReproSil-Pur C18) with the Whisper Zoom 40 samples-per-day method. Mobile phase A consisted of 0.1% formic acid in water, and mobile phase B consisted of 0.1% formic acid in acetonitrile. Peptides were separated using a 2–35% mobile phase B gradient. Data were acquired in dia-PASEF mode using TimsControl software [28]. MS acquisition was performed in positive ion mode over an m/z range of 100–1700, with 10 PASEF cycles per acquisition cycle. The CaptiveSpray voltage was set to 1,500 V, the capillary temperature to 180 °C, and the TOF acquisition rate to 10 kHz.

4.8 Proteomic data processing and bioinformatic analysis

Raw dia-PASEF files were processed using DIA-NN v1.9 in library-free mode against a *Homo sapiens* reference proteome database [29]. Searches were performed using tryptic specificity, allowing up to two missed cleavages. Carbamidomethylation of cysteine was set as a fixed modification, whereas methionine oxidation and protein N-terminal acetylation were included as variable modifications. DIA-NN protein inference and label-free quantification were performed using the standard DIA-NN workflow, and precursor-level identifications were controlled at 1% FDR. The protein abundance matrix exported from DIA-NN was used for downstream analysis in R. Reverse sequences, decoy entries, potential contaminants, and duplicated protein groups were removed before statistical analysis.

Because the culture medium contained fetal bovine serum, an additional peptide-level species specificity audit was performed using the UniProtKB reference proteomes of *Homo sapiens* (UP000005640) and *Bos taurus* (UP000009136), treating leucine and isoleucine as equivalent. Human-specific peptide support was assessed as the proportion of detected peptides unique to the human proteome and was considered when selecting representative proteins for biological interpretation. The primary quantitative differential abundance and enrichment analyses remained unchanged; species specificity was evaluated separately to assess potential bovine serum contributions.

Protein groups were retained for quantitative analysis when they were detected in at least 50% of samples in at least one experimental group. Analyses were performed separately for HeLa and SiHa cells to avoid confounding architecture-dependent differences with cell line-specific effects. Protein abundance values were log2-transformed, missing values were imputed using missForest v1.6.1 [41], and the resulting matrices were normalized by median adjustment across samples.

Quality control analyses included identification depth at the protein-group, peptide, and precursor levels; missing-value distribution; protein-intensity distribution; coefficient-of-variation analysis; principal component analysis; hierarchical clustering; and Spearman correlation analysis. Protein-level coefficients of variation were calculated within each experimental condition. Proteins with CV > 60% were excluded from CV visualization and average CV reporting. Principal component analysis and correlation analyses were performed independently for each cell line using the final processed quantitative matrices.

Architecture-associated detected protein subsets were evaluated in a qualitative presence/absence analysis using the non-imputed protein-level matrix, prior to quantitative retention, imputation, and median normalization. A protein was detected in each architecture when its LFQ intensity was greater than zero in at least one replicate of that architecture. Detected protein subsets were summarized across adherent, spheroid, and bioprinted models, including architecture-restricted subsets and pairwise overlaps. This presence/absence layer was analyzed separately from quantitative differential abundance testing.

Functional annotation of architecture-associated detected subsets was performed using MSigDB Hallmark gene sets and clusterProfiler. Over-representation analysis was performed separately for

each cell line using a one-sided hypergeometric test, with all proteins detected across the three architectures within that cell line as the background universe. P-values were adjusted using the Benjamini–Hochberg method. Enriched terms were interpreted as functional annotations of detected protein subsets rather than evidence of pathway activation.

Differential protein abundance analysis was performed using limma [42]. For each cell line and culture architecture, four wells were cultured independently and processed separately for proteomic analysis (n = 4 per condition), with each well constituting an individual experimental replicate. Linear models were fitted separately for each cell line to the processed protein abundance matrices, and empirical Bayes moderated statistics were used to evaluate the contrasts Sp *vs* Ad, Bp *vs* Ad, and Bp *vs* Sp. Differentially abundant proteins were defined using FDR < 0.05, without applying a fixed log2 fold-change cutoff. Positive log2 fold-change values indicate higher abundance in the first condition of each contrast.

Gene set enrichment analysis was performed using preranked protein-level statistics with fgsea [43]. Hallmark and GO Biological Process gene sets were used to evaluate pathway-signature-level patterns [44–46] across 3D *vs* adherent comparisons and direct Bp *vs* Sp contrasts. Enrichment results were summarized using normalized enrichment scores (NES). For fGSEA bubble plot visualizations, bubble color represented NES, and bubble size was scaled by $-\log10$(P-value). In the Hallmark NES heatmaps, significance was indicated using FDR thresholds: ***FDR < 0.01, **FDR < 0.1, *FDR < 0.25, and ns FDR $\geq$ 0.25. Enrichment patterns meeting FDR < 0.25 but not FDR < 0.05 were treated as exploratory. Selected Hallmark fGSEA results (16 prioritized gene sets), GO Biological Process fGSEA candidate results, and complementary enrichment analyses are provided in Supplementary Table S4.

Protein association networks were generated using STRING v12 [47]. Networks were constructed for bioprinted-associated detected proteins to evaluate whether architecture-associated subsets formed functionally connected groups. Network visualization was used as an exploratory protein association analysis and was not interpreted as evidence of pathway activation. For the selected protein-level assessment, normalized log2 LFQ values from the final imputed matrices were extracted for proteins representing the main architecture-associated modules. Within each cell line, Sp *vs* Ad and Bp *vs* Ad comparisons were evaluated using Welch's t-test with unequal variances.

P-values were used to annotate significance levels in the focused protein-level plots. This analysis was performed as a descriptive, protein-level summary of selected module-associated abundance patterns and was not intended as an independent validation of the global differential abundance results.

4.9 Use of AI-assisted tools

ChatGPT (OpenAI) was used to assist with language editing and manuscript organization. All content was reviewed and approved by the authors, who take full responsibility for the manuscript.

4.10 Data availability

The mass spectrometry proteomics data have been deposited to the ProteomeXchange Consortium via the PRIDE partner repository [48] under accession number PXD084972 and are publicly available at https://www.ebi.ac.uk/pride/archive/projects/PXD084972.

5 References

1. Bray F, Laversanne M, Sung H, Ferlay J, Siegel RL, Soerjomataram I, et al. Global cancer statistics 2022: GLOBOCAN estimates of incidence and mortality worldwide for 36 cancers in 185 countries. CA Cancer J Clin. 2024;74: 229–263. doi:10.3322/caac.21834

2. Wu J, Jin Q, Zhang Y, Ji Y, Li J, Liu X, et al. Global burden of cervical cancer: current estimates, temporal trend and future projections based on the GLOBOCAN 2022. J Natl Cancer Cent. 2025;5: 322–329. doi:10.1016/j.jncc.2024.11.006

3. Cohen PA, Jhingran A, Oaknin A, Denny L. Cervical cancer. Lancet. 2019;393: 169–182. doi:10.1016/S0140-6736(18)32470-X

4. Scherer WF, Syverton JT, Gey GO. Studies on the propagation *in vitro* of poliomyelitis viruses. IV. Viral multiplication in a stable strain of human malignant epithelial cells (strain HeLa) derived from an epidermoid carcinoma of the cervix. J Exp Med. 1953;97: 695–710. doi:10.1084/jem.97.5.695

5. Friedl F, Kimura I, Osato T, Ito Y. Studies on a new human cell line (SiHa) derived from carcinoma of uterus. I. Its establishment and morphology. Proc Soc Exp Biol Med. 1970;135: 543–545. doi:10.3181/00379727-135-35091a

6. Meissner JD. Nucleotide sequences and further characterization of human papillomavirus DNA present in the CaSki, SiHa and HeLa cervical carcinoma cell lines. J Gen Virol. 1999;80 (Pt 7): 1725–1733. doi:10.1099/0022-1317-80-7-1725

7. Pampaloni F, Reynaud EG, Stelzer EHK. The third dimension bridges the gap between cell culture and live tissue. Nat Rev Mol Cell Biol. 2007;8: 839–845. doi:10.1038/nrm2236

8. Yamada KM, Cukierman E. Modeling tissue morphogenesis and cancer in 3D. Cell. 2007;130: 601–610. doi:10.1016/j.cell.2007.08.006

9. Edmondson R, Broglie JJ, Adcock AF, Yang L. Three-dimensional cell culture systems and their applications in drug discovery and cell-based biosensors. Assay Drug Dev Technol. 2014;12: 207–218. doi:10.1089/adt.2014.573

10. Chaicharoenaudomrung N, Kunhorm P, Noisa P. Three-dimensional cell culture systems as an *in vitro* platform for cancer and stem cell modeling. World J Stem Cells. 2019;11: 1065–1083. doi:10.4252/wjsc.v11.i12.1065

11. Jubelin C, Muñoz-Garcia J, Griscom L, Cochonneau D, Ollivier E, Heymann M-F, et al. Three-dimensional *in vitro* culture models in oncology research. Cell Biosci. 2022;12: 155. doi:10.1186/s13578-022-00887-3

12. Sutherland RM. Cell and environment interactions in tumor microregions: the multicell spheroid model. Science. 1988;240: 177–184. doi:10.1126/science.2451290

13. Casciari JJ, Sotirchos SV, Sutherland RM. Variations in tumor cell growth rates and metabolism with oxygen concentration, glucose concentration, and extracellular pH. J Cell Physiol. 1992;151: 386–394. doi:10.1002/jcp.1041510220

14. Hirschhaeuser F, Menne H, Dittfeld C, West J, Mueller-Klieser W, Kunz-Schughart LA. Multicellular tumor spheroids: an underestimated tool is catching up again. J Biotechnol. 2010;148: 3–15. doi:10.1016/j.jbiotec.2010.01.012

15. Riffle S, Hegde RS. Modeling tumor cell adaptations to hypoxia in multicellular tumor spheroids. J Exp Clin Cancer Res. 2017;36: 102. doi:10.1186/s13046-017-0570-9

16. Amemiya T, Shibata K, Takahashi J, Watanabe M, Nakata S, Nakamura K, et al. Glycolytic oscillations in HeLa cervical cancer cell spheroids. FEBS J. 2022;289: 5551–5570. doi:10.1111/febs.16454

17. Marín-Hernández A, Gallardo-Pérez JC, Ralph SJ, Rodríguez-Enríquez S, Moreno-Sánchez R. HIF-1alpha modulates energy metabolism in cancer cells by inducing over-expression of specific glycolytic isoforms. Mini Rev Med Chem. 2009;9: 1084–1101. doi:10.2174/138955709788922610

18. Monteiro MV, Gaspar VM, Ferreira LP, Mano JF. Hydrogel 3D *in vitro* tumor models for screening cell aggregation mediated drug response. Biomater Sci. 2020;8: 1855–1864. doi:10.1039/c9bm02075f

19. Mondal A, Gebeyehu A, Miranda M, Bahadur D, Patel N, Ramakrishnan S, et al. Characterization and printability of Sodium alginate -Gelatin hydrogel for bioprinting NSCLC co-culture. Sci Rep. 2019;9: 19914. doi:10.1038/s41598-019-55034-9

20. Flores-Torres S, Peza-Chavez O, Kuasne H, Munguia-Lopez JG, Kort-Mascort J, Ferri L, et al. Alginate-gelatin-Matrigel hydrogels enable the development and multigenerational passaging of patient-derived 3D bioprinted cancer spheroid models. Biofabrication. 2021;13: 025001. doi:10.1088/1758-5090/abdb87

21. Zhao Y, Yao R, Ouyang L, Ding H, Zhang T, Zhang K, et al. Three-dimensional printing of Hela cells for cervical tumor model *in vitro*. Biofabrication. 2014;6: 035001. doi:10.1088/1758-5082/6/3/035001

22. Pang Y, Mao SS, Yao R, He JY, Zhou ZZ, Feng L, et al. TGF-β induced epithelial–mesenchymal transition in an advanced cervical tumor model by 3D printing. Biofabrication. 2018;10: 044102. doi:10.1088/1758-5090/aadbde

23. Othman SA, Soon CF, Ma NL, Tee KS, Lim GP, Morsin M, et al. Alginate-gelatin bioink for bioprinting of hela spheroids in alginate-gelatin hexagon shaped scaffolds. Polym Bull (Berl). 2021;78: 6115–6135. doi:10.1007/s00289-020-03421-y

24. Becconi M, De Zio S, Falciani F, Santamaria M, Malferrari M, Rapino S. Nano-electrochemical characterization of a 3D bioprinted cervical tumor model. Cancers (Basel). 2023;15: 1327. doi:10.3390/cancers15041327

769 25. Aebersold R, Mann M. Mass-spectrometric exploration of proteome structure and function.
770 Nature. 2016;537: 347–355. doi:10.1038/nature19949

771 26. Cristobal A, van den Toorn HWP, van de Wetering M, Clevers H, Heck AJR, Mohammed S.
772 Personalized proteome profiles of healthy and tumor human colon organoids reveal both individual
773 diversity and basic features of colorectal cancer. Cell Rep. 2017;18: 263–274.
774 doi:10.1016/j.celrep.2016.12.016

775 27. Hughes CS, Foehr S, Garfield DA, Furlong EE, Steinmetz LM, Krijgsveld J. Ultrasensitive
776 proteome analysis using paramagnetic bead technology. Mol Syst Biol. 2014;10: 757.
777 doi:10.15252/msb.20145625

778 28. Meier F, Brunner A-D, Frank M, Ha A, Bludau I, Voytik E, et al. diaPASEF: parallel
779 accumulation-serial fragmentation combined with data-independent acquisition. Nat Methods.
780 2020;17: 1229–1236. doi:10.1038/s41592-020-00998-0

781 29. Demichev V, Messner CB, Vernardis SI, Lilley KS, Ralser M. DIA-NN: neural networks and
782 interference correction enable deep proteome coverage in high throughput. Nat Methods. 2020;17:
783 41–44. doi:10.1038/s41592-019-0638-x

784 30. Leek RD, Stratford I, Harris AL. The role of hypoxia-inducible factor-1 in three-dimensional
785 tumor growth, apoptosis, and regulation by the insulin-signaling pathway. Cancer Res. 2005;65:
786 4147–4152. doi:10.1158/0008-5472.CAN-04-2184

787 31. Rodríguez-Enríquez S, Gallardo-Pérez JC, Avilés-Salas A, Marín-Hernández A, Carreño-
788 Fuentes L, Maldonado-Lagunas V, et al. Energy metabolism transition in multi-cellular human
789 tumor spheroids. J Cell Physiol. 2008;216: 189–197. doi:10.1002/jcp.21392

790 32. Li F, Zhang Y, Wu C. Integrin-linked kinase is localized to cell-matrix focal adhesions but not
791 cell-cell adhesion sites and the focal adhesion localization of integrin-linked kinase is regulated by
792 the PINCH-binding ANK repeats. J Cell Sci. 1999;112 (Pt 24): 4589–4599.
793 doi:10.1242/jcs.112.24.4589

794 33. Tu Y, Li F, Goicoechea S, Wu C. The LIM-only protein PINCH directly interacts with integrin-
795 linked kinase and is recruited to integrin-rich sites in spreading cells. Mol Cell Biol. 1999;19:
796 2425–2434. doi:10.1128/MCB.19.3.2425

797 34. Legate KR, Montañez E, Kudlacek O, Fässler R. ILK, PINCH and parvin: the tIPP of integrin
798 signalling. Nat Rev Mol Cell Biol. 2006;7: 20–31. doi:10.1038/nrm1789

799 35. Górska A, Mazur AJ. Integrin-linked kinase (ILK): the known *vs.* the unknown and
800 perspectives. Cell Mol Life Sci. 2022;79: 100. doi:10.1007/s00018-021-04104-1

801 36. Greco MR, Moro L, Forciniti S, Alfarouk K, Cannone S, Cardone RA, et al. Integrin-linked
802 kinase links integrin activation to invadopodia function and invasion via the p(T567)-
803 ezrin/NHERF1/NHE1 pathway. Int J Mol Sci. 2021;22: 2162. doi:10.3390/ijms22042162

804 37. Persad S, Dedhar S. The role of integrin-linked kinase (ILK) in cancer progression. Cancer
805 Metastasis Rev. 2003;22: 375–384. doi:10.1023/a:1023777013659

806 38. Lima LG, Monteiro RQ. Activation of blood coagulation in cancer: implications for tumour
807 progression. Biosci Rep. 2013;33: e00064. doi:10.1042/BSR20130057

808 39. Wojtukiewicz MZ, Hempel D, Sierko E, Tucker SC, Honn KV. Thrombin-unique coagulation
809 system protein with multifaceted impacts on cancer and metastasis. Cancer Metastasis Rev.
810 2016;35: 213–233. doi:10.1007/s10555-016-9626-0

811 40. Reddel CJ, Allen JD, Ehteda A, Taylor R, Chen VMY, Curnow JL, et al. Increased thrombin
812 generation in a mouse model of cancer cachexia is partially interleukin-6 dependent. J Thromb
813 Haemost. 2017;15: 477–486. doi:10.1111/jth.13612

814 41. Stekhoven DJ, Bühlmann P. MissForest--non-parametric missing value imputation for mixed-
815 type data. Bioinformatics. 2012;28: 112–118. doi:10.1093/bioinformatics/btr597

816 42. Ritchie ME, Phipson B, Wu D, Hu Y, Law CW, Shi W, et al. limma powers differential
817 expression analyses for RNA-sequencing and microarray studies. Nucleic Acids Res. 2015;43: e47.
818 doi:10.1093/nar/gkv007

819 43. Korotkevich G, Sukhov V, Budin N, Shpak B, Artyomov M, Sergushichev A. Fast gene set
820 enrichment analysis. bioRxiv. bioRxiv; 2016. doi:10.1101/060012

821 44. Subramanian A, Tamayo P, Mootha VK, Mukherjee S, Ebert BL, Gillette MA, et al. Gene set
822 enrichment analysis: a knowledge-based approach for interpreting genome-wide expression
823 profiles. Proc Natl Acad Sci U S A. 2005;102: 15545–15550. doi:10.1073/pnas.0506580102

45. Liberzon A, Birger C, Thorvaldsdóttir H, Ghandi M, Mesirov JP, Tamayo P. The Molecular Signatures Database (MSigDB) hallmark gene set collection. Cell Syst. 2015;1: 417–425. doi:10.1016/j.cels.2015.12.004

46. Gene Ontology Consortium. The Gene Ontology knowledgebase in 2026. Nucleic Acids Res. 2026;54: D1779–D1792. doi:10.1093/nar/gkaf1292

47. Szklarczyk D, Nastou K, Koutrouli M, Kirsch R, Mehryary F, Hachilif R, et al. The STRING database in 2025: protein networks with directionality of regulation. Nucleic Acids Res. 2025;53: D730–D737. doi:10.1093/nar/gkae1113

48. Perez-Riverol Y, Bandla C, Kundu DJ, Kamatchinathan S, Bai J, Hewapathirana S, et al. The PRIDE database at 20 years: 2025 update. Nucleic Acids Res. 2025;53: D543–D553. doi:10.1093/nar/gkae1011

Acknowledgments: The authors acknowledge the support of the Laboratorio de Biotecnología y Biofármacos, Universidad de Concepción, and MELISA Institute during the development of this study.

Author Contributions: Conceptualization: P.S., J.T.; Methodology: P.S., F.V.-A., C.V., M.J.L.-C., S.H., R.L.; Software: P.S.; Formal analysis: P.S.; Investigation: P.S., F.V.-A., C.V., M.J.L.-C., S.H., R.L.; Resources: M.H., J.T., R.L.; Data curation: P.S.; Writing – original draft: P.S.; Writing – review & editing: P.S., F.V.-A., C.V., M.J.L.-C., S.H., R.L., E.G., R.S.M., M.H., J.T.; Visualization: P.S.; Supervision: J.T., M.H.; Project administration: P.S., M.H., J.T.; Funding acquisition: P.S., M.H., J.T. All authors have read and approved the final version of the manuscript.

Conflicts of interest: The authors declare no competing interests.

Funding: This research was supported by FIC-R BIP 40036149-0, the FISAR Foundation, grant number CLA042024-01, and the PhD Program in Molecular Biotechnology at the University of Concepción, code 4244. P.S. was supported by ANID — Agencia Nacional de Investigación y Desarrollo, Subdirección de Capital Humano, Doctorado Nacional 2023, PhD grant number 21231852.

Table 1. Representative architecture-skewed proteins distinguishing spheroid and bioprinted cervical cancer models.

Module	Protein	Protein description	log2FC Sp *vs* Ad HeLa	log2FC Sp *vs* Ad SiHa	log2FC Bp *vs* Ad HeLa	log2FC Bp *vs* Ad SiHa	log2FC Bp *vs* Sp HeLa	log2FC Bp *vs* Sp SiHa
Metabolic / hypoxia-associated	ENO1	Alpha-enolase; glycolytic enzyme	1.30	1.37	-1.51	-0.27	-2.82	-1.64
	ENO2	Enolase 2; glycolytic enzyme	1.86	2.69	-0.59	-0.70	-2.45	-3.39
	TPI1	Triosephosphate isomerase; glycolytic enzyme	1.41	1.44	-0.97	-0.09	-2.38	-1.53
ECM remodeling / cell-matrix interaction	VTN	Vitronectin; ECM glycoprotein	3.74	3.55	6.29	8.36	2.55	4.81
	TIMP2	Metalloproteinase inhibitor; ECM remodeling	0.35	0.19	1.95	4.28	1.60	4.09
	ILK	Integrin-linked cell-matrix protein	-0.20	-0.06	0.89	1.24	1.10	1.31
Extracellular remodeling	ITIH2	Inter-alpha-trypsin inhibitor heavy chain 2; ECM remodeling	3.67	3.16	4.59	7.37	0.92	4.21
	C3	Complement C3; central complement component	3.65	1.78	4.36	4.95	0.71	3.17
	CD47	Leukocyte surface antigen CD47; integrin-associated	2.17	1.93	2.43	2.98	0.26	1.05
	CLU	Clusterin; extracellular chaperone / proteostasis	2.03	2.25	1.55	0.59	-0.48	-1.66

* Values are shown as log2 fold-change. Positive values indicate higher abundance in the first condition of each contrast. For the Bp *vs* Sp contrast, positive values indicate higher abundance in bioprinted models, whereas negative values indicate higher abundance in spheroids. Proteins are grouped according to their associated functional module. Proteins were selected to represent architecture-associated abundance patterns across the three functional modules. Statistical significance in the direct Bp *vs* Sp comparison varied between cell lines. Significant differential abundance results are provided in Supplementary Table S3.

Table 2. Representative Hallmark enrichment patterns across spheroid and bioprinted cervical cancer models.

Module	Hallmark term	NES Sp *vs* Ad HeLa	NES Sp *vs* Ad SiHa	NES Bp *vs* Ad HeLa	NES Bp *vs* Ad SiHa
Metabolic / hypoxia-associated	Oxidative phosphorylation	2.92	1.78	1.94	1.52
	Glycolysis	1.93	2.25	-1.52	1.13 (ns)
	Hypoxia	2.03	2.11	-1.21 (ns)	-1.14 (ns)
ECM remodeling / cell-matrix interaction	Epithelial mesenchymal transition	2.38	2.29	1.57	1.76
Extracellular remodeling	Coagulation	2.58	2.33	2.37	2.29
	Complement	2.29	1.80	1.55	1.66

* NES, normalized enrichment score. Positive NES values indicate higher representation in the 3D condition relative to adherent cultures for each contrast, whereas negative NES values indicate lower representation in the 3D condition. Values marked as 'ns' did not meet the displayed FDR < 0.25 threshold. Additional results for the prioritized Hallmark gene sets, including nominal and adjusted P-values, are provided in Supplementary Table S4.

Supplementary Files

This is a list of supplementary files associated with this preprint. Click to download.

- SupplementaryTableS1.xlsx
- SupplementaryTableS5.xlsx
- SupplementaryTableS4.xlsx
- SupplementaryTableS2.xlsx
- SupplementaryTableS3.xlsx
- SupplementaryInformationv1.pdf